



Mutual promotion by structural design and intrinsic activity coupling of CNTs/MoC/CoNiMo for water splitting and urea electrolysis

Xuesong Liu^a, Kuan Deng^a, Peng Liu^a, Xingbin Lv^b, Wen Tian^a, Kui Ma^a, Hongjiao Li^{a,*}, Junyi Ji^{a,c,**}

^a School of Chemical Engineering, Sichuan University, Chengdu 610065, PR China

^b College of Chemistry and Environment, Southwest Minzu University, Chengdu, Sichuan 610041, PR China

^c State Key Laboratory of Polymer Materials Engineering, Sichuan University, Chengdu 610065, PR China



ARTICLE INFO

Keywords:

Carbon nanotube
Nanostructures
Integrated tri-functional heterostructure
In-situ catalytic growth
Water splitting

ABSTRACT

Construction of durable multi-function electrocatalysts for hydrogen production is still highly challenging. Herein, we report a hierarchical integrated tri-functional heterogeneous CNTs/MoC/CoNiMo electrode for HER and related OER/UOR. The carbon-protected Ni nanoparticles yield abundant γ -NiOOH active intermediates to boost OER/UOR, while DFT calculations verify Mo migration induced by MoC and CoNiMo alloy under negative potentials generates HER super-active sites on Mo-rich surfaces. Additionally, the parallel aligned nanosheets with out-plane extended CNTs arrays can guide the rapid bubbles release and expand the accessible surface area. Therefore, the optimized CNT/MoC/NMC-3 electrode can achieve overpotentials of 51 mV (HER) and 226 mV (OER), with low potential threshold of 1.257 V (UOR) at 10 mA cm^{-2} . Moreover, the assembled symmetric urea electrolyzer reaches a 1.291 V cell voltage at 10 mA cm^{-2} . This work provides a novel strategy for heterostructure multi-component integration for achieving high-efficiency hydrogen production and urea-containing wastewater purification.

1. Introduction

Hydrogen with high energy density and pollution-free nature is considered as the most potential alternative sustainable energy to alleviate the energy crisis and environmental pollution [1]. Water electrolysis driven by renewable energy is an economical route with zero-carbon-emission conversion [2]. However, a considerable overpotential is generally required in practical applications of hydrogen production due to the sluggish four-electron anodic oxygen evolution reaction (OER) kinetics. Therefore, the design of the efficient electrocatalysts is still challenging to achieve high electrocatalytic activity and durability.

To address the bottleneck, the development of electrocatalysts with low activation energy barriers, accelerated reaction kinetics, robust structural stability and sufficient exposed active sites is essential [3,4]. Generally, noble metals such as Pt- and Ru/Ir-based compounds exhibit the first-rate activities towards hydrogen evolution reaction (HER) and OER, respectively, but the scarcity and high price have limited their

practical application. Therefore, developing cost-effective electrocatalysts with comparable activity or lower noble metal content becomes highly imperative [5–10]. Recently, transition-metal based alloys and their compounds with non-metallic elements have been widely investigated due to the balanced electronic structure and synergistically-enhanced reaction kinetics in water splitting [11,12]. Wu *et al.* demonstrate a heterogeneous Ni-MoN electrocatalyst consisting metallic Ni and MoN nanoparticles on amorphous MoN nanorods, which can achieve remarkable HER performance with ultralow overpotentials of 61 mV and 136 mV to drive 100 mA cm^{-2} and 1000 mA cm^{-2} , respectively [13]. Furthermore, constructing ordered and stable micro-structures is another keypoint to promote electrolyte infiltration and gas release [14], which can reduce the “dead volume” and increase the accessible active site density [15]. Zhang *et al.* synthesized a 3D core-shell electrocatalyst consisting of Co(OH)_2 cavity array-encapsulated NiMo alloy on carbon cloth. Benefiting from the open porous structure of the outer Co(OH)_2 array and the multiple active sites at $\text{Co(OH)}_2/\text{NiMo}$ heterogeneous interface, the electrocatalyst

* Corresponding author.

** Corresponding author at: School of Chemical Engineering, Sichuan University, Chengdu 610065, PR China.

E-mail addresses: hongjiao.li@scu.edu.cn (H. Li), junyiji@scu.edu.cn (J. Ji).

delivers a low cell voltage of 1.52 V at 10 mA cm⁻² in overall water splitting [16].

In addition, the optimization of electrolysis system is another key factor to raise the hydrogen production efficiency and reduce energy consumption [17]. Recently, replacement of the anodic OER process with more readily oxidizable substances including methanol [18], urea [19,20], hydrazine [21], etc., can reduce the thermodynamic voltage required and accelerate reaction kinetics. Among them, urea oxidation reaction (UOR) with low theoretical potential of 0.37 V is attractive process comparing with that of OER (1.23 V vs. RHE). This is especially significant because urea is a potentially free source derived from human urine and urea-rich agricultural wastewater [22,23], which further emphasize the significant potential of UOR process to lower hydrogen production costs and enhance environmental friendliness of the integrated electrocatalytic system [24]. The use of urea thus combines environmental benefits with cost-efficiency. However, UOR is intrinsically sluggish due to the six-electron transfer process. Nickel-based catalysts have been studied as alternatives to noble metals for UOR. Jia *et al.* synthesized an electrocatalyst composed of amorphous Ni(OH)S nanosheets with Ni³⁺-rich phases, which can accelerate the reaction kinetics. The electrocatalyst can achieve low overpotentials of 250 mV and 110 mV toward the OER and UOR at 10 mA cm⁻² [25]. Nonetheless, there is still a challenge to produce multi-component Ni-based electrocatalysts with enhanced reaction kinetics and well-designed 3D nanostructure to achieve high-performance HER and UOR/OER.

Herein, an in-situ growth strategy of CNTs arrays on the parallel aligned NiMoO₄ precursors is reported by one-step chemical vapor deposition (CVD) method, the programmed annealing treatment process enables the preparation of this tightly integrated hierarchical CNTs/MoC/CoNiMo alloy (CNT/MoC/NMC) heterostructure. The active phases evolution and mutual activity coupling under various potentials during electrocatalysis are monitored by ex-situ and in-situ techniques. The Ni nanoparticles with the protective graphite carbon coating possesses great activity and stability, which can accelerate the γ -NiOOH active intermediate formation and stably drive the OER/UOR. DFT calculations have confirmed that MoC and CoNiMo alloy can induce the Mo elements migration to the outer surface under negative potentials, resulting in thermodynamically stable and HER active Mo-surf.-rich surface with an energy difference at least 1.1 eV lower than other systems. Moreover, the out-plane extended CNTs and parallel aligned nanosheets structure can expand the accessible surface area and accelerate the rapidly bubbles release. Therefore, the optimized CNT/MoC/NMC-3 electrode can achieve low overpotential of 51 mV and 226 mV at 10 mA cm⁻² toward the HER and OER, respectively. In addition, the anodic replacement reaction can achieve an exceptional UOR activity of 1.257 V at 10 mA cm⁻², which is 0.199 V lower than that of the OER. When assembling CNT/MoC/NMC-3 into a symmetric electrolyzer, the cell voltage reduces to 1.291 V at 10 mA cm⁻² to electrolyze urea and can be driven by a 1.5 V button battery.

2. Experimental section

2.1. Preparation of NiMoO₄/CoCH

All the raw materials purchased from Aladdin Co. were used directly without any further purification. The heterostructures of NiMoO₄ nanosheets assembled on Co(CO₃)_{0.5}(OH)•0.11 H₂O (CoCH) nano-needles were fabricated by a two-step hydrothermal treatment according to our previously reported using conductive carbon cloth as the substrate (denoted as NiMoO₄/CoCH) [26,27].

2.2. Preparation of CNT/MoC/NMC-x

The NiMoO₄/CoCH precursors catalyzed in-situ growth of nitrogen-doped CNTs were conducted in a tube furnace. Firstly, the NiMoO₄/CoCH composite was calcinated from room temperature to 450 °C with a

heating rate of 4 °C min⁻¹ in a H₂/Ar (10:90) atmosphere and kept for 1.5 h. Then, the pre-reduced composite was heated to 600 °C rapidly within 10 min under the same atmosphere. After that, the Ar was cut off and the H₂, C₂H₂, and NH₃ mixture (1:1:0.5) was injected for different periods (1, 2, 3, 5, and 10 min) under 200 mbar. Finally, the H₂, C₂H₂, and NH₃ was cut off and Ar was injected and cool naturally to room temperature to obtain the CNT/MoC/NMC-x ($x = 1, 2, 3, 5$, and 10 min).

2.3. Preparation of CNT/MoC/NMC-n

The effect of reaction temperature on the catalytic growth of carbon nanotubes was compared. The reaction conditions were consistent with the previous step and the reaction time is 3 min, and set the temperature for the growth of carbon nanotubes as 500, 550, 600, 650, and 700 °C, and denoted it as CNT/MoC/NMC-n ($n = 500, 550, 600, 650$, and 700 °C).

3. Results and discussion

3.1. Synthesis and structural characterization

The schematics for the synthesis of the CNT/MoC/NMC composites are shown in Fig. 1a, which include a two-step hydrothermal treatment and CVD process. Firstly, a heterostructure consist of parallel aligned NiMoO₄ nanosheet arrays along the axial direction of the CoCH nano-needle arrays on carbon cloth is fabricated (Fig. S1) [27]. Secondly, through a one-step CVD calcination method, the active metal seeds are formed on the NiMoO₄ precursor and the CNTs arrays are catalytic grown on the out-plane of the nanosheets. Fig. 1b illustrates the schematic diagram of the surface restructuring and CNTs growth process of the NiMoO₄ nanosheet. The Ni atoms can be extruded from NiMoO₄ host lattice under thermal-activation and reduction environment, thus form the dispersed Ni nanoparticles and MoO₂ on the surface. Then, after rise the temperature to 600 °C and the introduction of reaction gases, the Ni seeds and active metal species can directly decompose C₂H₂ to grow CNTs and encapsulated carbon layers. The H₂ and NH₃ can provide reduction atmosphere and nitrogen source to increase the crystallinity and produce more defects and electronic dislocations, which can increase the intrinsic electron conductivity, as well as significantly improves the surface hydrophilicity to facilitate the electrolyte infiltration and active sites exposure. Meanwhile, the MoO₂ can be carbonized to MoC under the relatively low temperature (Table S1). This may be attributed to the high catalytic cracking reactivity of the well-dispersed ultrasmall Ni nanoparticles reduced from NiMoO₄ nanosheets, confirming the advantageous of continuous reaction process in which such seed crystals are in-situ generated from the substrate. Moreover, the CoCH together with NiMoO₄ can form tri-metallic alloy, which enables uniform dispersion of the surface-loaded MoC and CNTs. In the fabrication process, the crystal seeds in-situ generated from the substrate with continuous reaction process is extremely advantageous to evolve heterogeneous structure with tightly interface [28]. In addition, the low-pressure reaction can effectively accelerate the mass transfer between carbonaceous species and metallic catalytic sites for rapid CNTs growth, thus eliminating the potential risk of structural deformation caused by prolonged exposure under high temperature.

X-ray diffraction (XRD) is applied to provide the crystalline evolution process. As shown in Fig. 1c, the peaks belonging to the NiMoO₄ and CoCH disappear after reduction by H₂ (Fig. S2), while the presence of new peaks located at 44.5°, 51.9°, and 76.4° correspond to the metallic Ni (JCPDS 87-0712). Moreover, the peaks located at 37.0° and 41.4° are attributed to the (-211) and (210) planes of MoO₂ (JCPDS 32-0671), while the peaks shift to 36.8°, 39.3°, and 61.5° when reaction is extended to 3 or 5 min, which corresponds to the (006), (103), and (110) planes of MoC (JCPDS 08-0384). Furthermore, within 1 min reaction, the wide peak near 43° may be attributed to the mixed peak of metallic Ni and the tri-metallic alloy of Co_{1.3}Ni_{4.1}Mo_{4.6} with low crystallinity

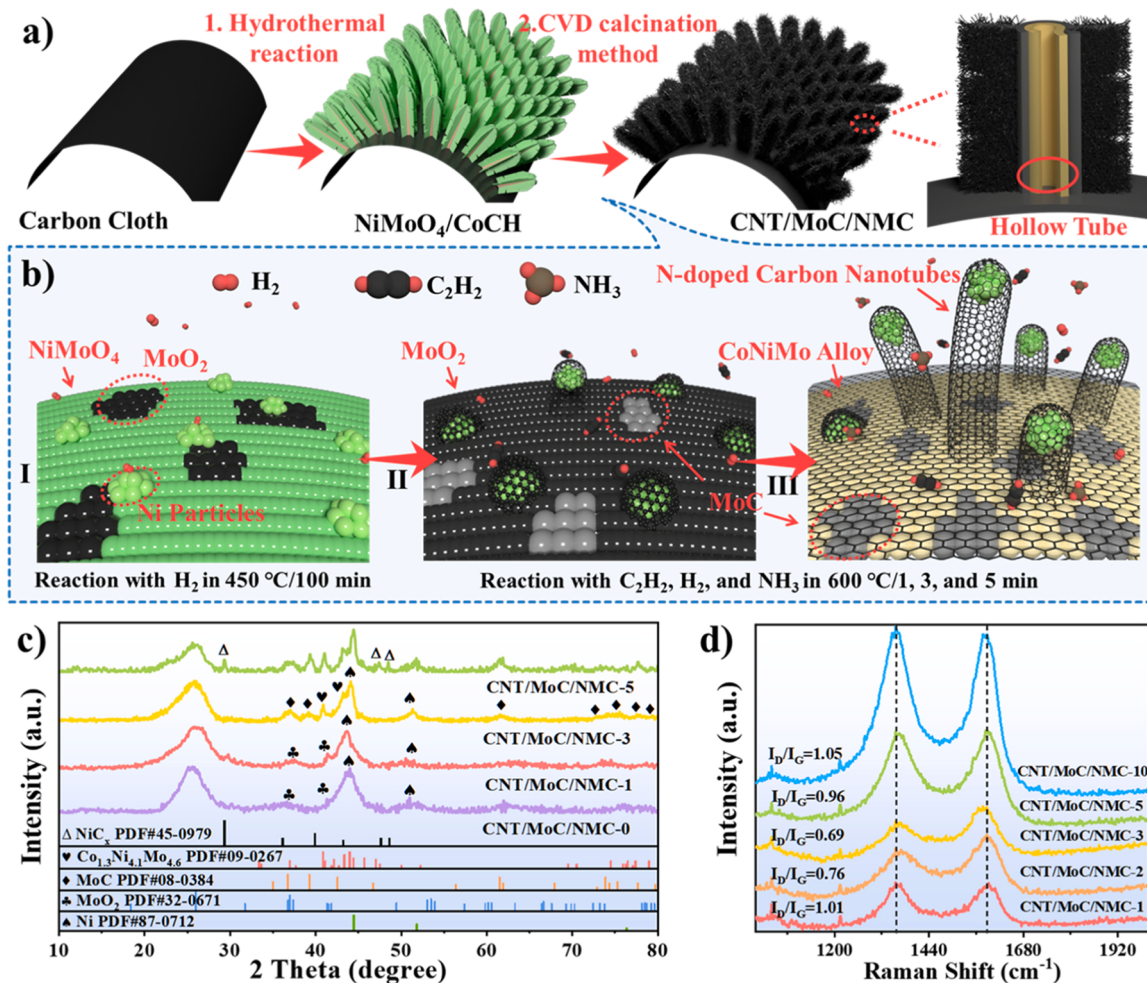


Fig. 1. (a) Schematic illustration of the synthesis process of CNT/MoC/NMC. (b) Schematic diagram of surface reconstruction and CNTs growth during CVD process. (c) XRD patterns and (d) Raman spectra of the CNT/MoC/CoCH-x composites.

(JCPDS 09-0267). With the extension of treatment time, the peaks centered at 40.9° and 43.4° belongs to Co_{1.3}Ni_{4.1}Mo_{4.6} appear. The tri-metallic alloy possesses good electrical conductivity, and can form Co- and Mo-doped NiOOH intermediate with high electrocatalysis activity in alkaline solution [29]. Meanwhile, the peaks located at 29.4°, 47.7°, and 48.6° of CNT/MoC/NMC-5 correspond to the signal of NiC_x (JCPDS 45-0979). Furthermore, the graphitization degree of the CNTs and carbon coating is evaluated by Raman spectroscopy. The calculated I_D/I_G values of the CNT/MoC/NMC-1, 2, 3, 5, and 10 are 1.01, 0.76, 0.69, 0.96, and 1.05 (Fig. 1d), respectively, thus the reaction period of 3 min leads to a higher graphitization degree. Too short growth time is not enough for the orderly extension of CNTs arrays, while too long period may accumulate amorphous carbon on the CNTs surface.

The surface reconstruction and structural evolution is investigated by scanning electron microscopy (SEM). After calcined under 450 °C, the long-range quasi-two-dimensional morphology remains unchanged (Fig. S3), indicating the robust thermostability of the hierarchical heterostructure. Moreover, massive nanoparticles can be observed on the composite surface (Fig. S3f) with obviously magnetic nature after H₂ reduction (Video S1), verifying the formation of tri-metallic alloy and monodispersed Ni nanoparticles. The effect of reaction time to the CNTs length and composite morphology is also evaluated (Fig. 2 and S4). Within 2 min, the CNTs are inconspicuous and unevenly distributed on nanosheet surface. When growth more than 5 min, the parallel aligned precursor structure is completely disappeared, which significantly reduces the spatial utilization and increases amorphous carbon

accumulation. After 3 min growth, the vertically and densely distributed CNTs arrays on MoC/NMC can be observed, which can effectively promote the electrolyte infiltration, enlarge accessible surface area and build multi-dimensional electron transfer network. In addition, benefiting from the superhydrophilic nature of the surface caused by nitrogen doping, the out-plane extended CNTs arrays can guide the rapid release of the generated gas bubbles and enhance the re-exposure of electrocatalytic active sites. This can be confirmed by its noticeably smaller and uniform dispersed bubbles generated under high current density of 200 mA cm⁻² compared to the unloaded CNTs sample, as well as the smaller water contact angle. (Fig. 2g, h, see Video S2 for dynamic details). Accordingly, the corresponding EDS mapping shows the uniform distribution of the elements along the carbon fiber (Fig. S5).

Transmission electron microscopy (TEM) is utilized to investigate the multi-component structure of CNT/MoC/NMC-3 composite. The average CNTs diameter is about 15 nm with Ni nanoparticles encapsulated on the top (Fig. 3a, b). Moreover, due to the reduction under high temperature, the CoCH is decomposed to release H₂O and CO₂, while thermally-driven outward migration and eutectic with Ni and Mo species on the surface to form a hollow tri-metallic alloy. Moreover, the hollow structure can enlarge the available electrochemical active area (Fig. S6), thus accelerate active intermediates formation in the electrocatalytic process [30]. The lattice fringes with interplanar spacings of 0.232, 0.209, and 0.218 nm are detected (Fig. 3c), which belong to metallic Ni, MoC, and Co_{1.3}Ni_{4.1}Mo_{4.6}, respectively. Meanwhile, the heterogeneous structure of coexisted multicomponent can also be

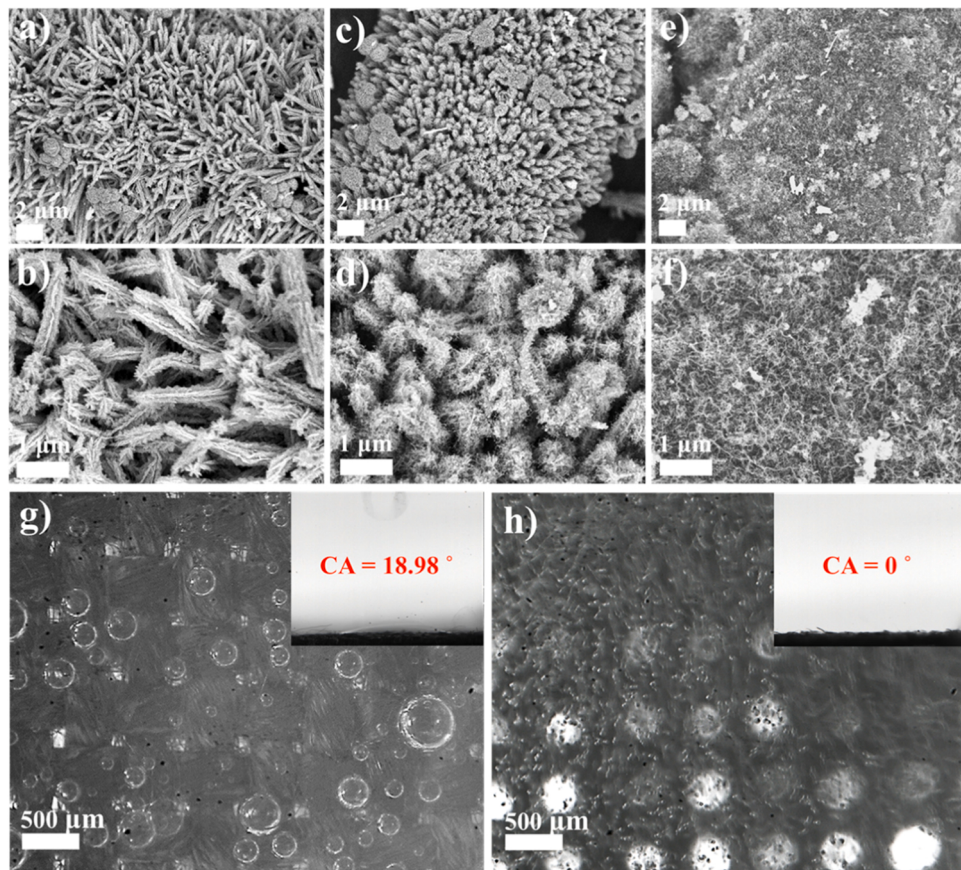


Fig. 2. SEM images of the (a, b) CNT/MoC/NMC-1, (c, d) CNT/MoC/NMC-3, and (e, f) CNT/MoC/NMC-5, optical images of the bubble release and related water contact angles (illustration in top right corner) of the (g) NiMoO₄/CoCH and (h) CNT/MoC/NMC-3 composites.

verified by various detailed surface crystalline and elemental distribution mapping/line scan (Fig. 3i, S7, and S8). The selected area electron diffraction (SAED) patterns also confirm the existence of these three phases (Fig. 3g, h). Furthermore, the corresponding fast Fourier transform (FFT) and inverse FFT patterns of the selected areas contain abundant edge dislocations and lattice distortions (Fig. 3c, e, and f). These defects can provide numerous electrocatalytic active sites whereas avoiding the aggregation of supported nanoparticles [31], thus revealing the strongly coupled heterointerfaces between species. The metallic Ni nanoparticles exhibit excellent crystallinity due to the high temperature treatment, as evidenced by the corresponding FFT pattern in Fig. 3c. In addition, the Ni particles inside the CNTs exhibit a crystal spacing of 0.203 nm, corresponding to the (111) plane of metallic nickel (Fig. 3d). While the interplanar spacing of 0.341 nm belongs to the graphitic carbon, verifying that the Ni nanoparticles are encapsulated by the graphitic carbon layer with a thickness of 1–2 nm. The intimate and ultrathin encapsulation of well-graphitized carbon can not only enhance the structural stability and electrical conductivity, but also profit from the spillover effect of heterogeneous catalysts, thus this “core-shell” structure can modify the number of active sites on the graphitized carbon surface [32,33].

3.2. Electrochemical properties

3.2.1. HER and OER catalytic performance

To investigate the HER activities of the electrocatalysts, the linear sweep voltammetry (LSV) curves are tested at 2 mV s⁻¹ with *iR* correction. The NiMoO₄/CoCH exhibits an overpotential of 317 mV for HER at 10 mA cm⁻² (Fig. 4a), while the composites exhibit enhanced electrocatalytic ability with overpotentials of 189, 89, 51, 122, and 141 mV at

10 mA cm⁻² for CNT/MoC/NMC-1, CNT/MoC/NMC-2, CNT/MoC/NMC-3, CNT/MoC/NMC-5, and CNT/MoC/NMC-10, respectively. Especially, the optimized CNT/MoC/NMC-3 reveals superior electroactivity with an overpotential of 140 mV under 200 mA cm⁻², even better than that of the commercial Pt/C (192 mV). The Tafel slope of the CNT/MoC/NMC-3 is calculated to be 66.08 mV dec⁻¹ (Fig. 4b), which is lower than NiMoO₄/CoCH (120.65 mV dec⁻¹) and other CNT/MoC/NMC-x electrodes. Furthermore, the electrochemical active surface areas (ECSA) are determined by calculating the double-layer capacitance (*C*_{dl}, Fig. 4g, S9, and S10). The *C*_{dl} value increases significantly from 3.93 mF cm⁻² of NiMoO₄/CoCH to 55.63 mF cm⁻² of CNT/MoC/NMC-3, indicating the large accessible surface area due to the multi-component interfaces and the extended CNTs arrays. The superior HER activity may benefit from the accelerated reaction kinetics of well-designed MoC and CoNiMo alloy in alkaline solution, while the hierarchical heterostructure and well-distributed active species can promote the electrolyte infiltration and intrinsic activity. Moreover, the uniform CNTs can effectively separate the generated bubbles rapidly and facilitate the re-exposure of the active sites, especially under high current density, thus enhancing the HER stability.

Moreover, as the CNT/MoC/NMC-x composites consist of multiple active sites, the OER can be occurred rapidly driven by the coupled active components. As shown in Fig. 4d, the optimal CNT/MoC/NMC-3 electrode reveals a relatively low overpotential of 226 mV at 10 mA cm⁻² for OER, which is superior than the benchmark IrO₂ catalyst (243 mV). A clear oxidation peak can be observed at around 1.3–1.4 V (vs. RHE), which can be ascribed to the oxidation of Ni⁰ species in Ni-based catalysts to form NiOOH [34]. In comparison, the oxidation peak of the NiMoO₄/CoCH precursor is difficult to be distinguished, demonstrating that the highly active metallic Ni inside the

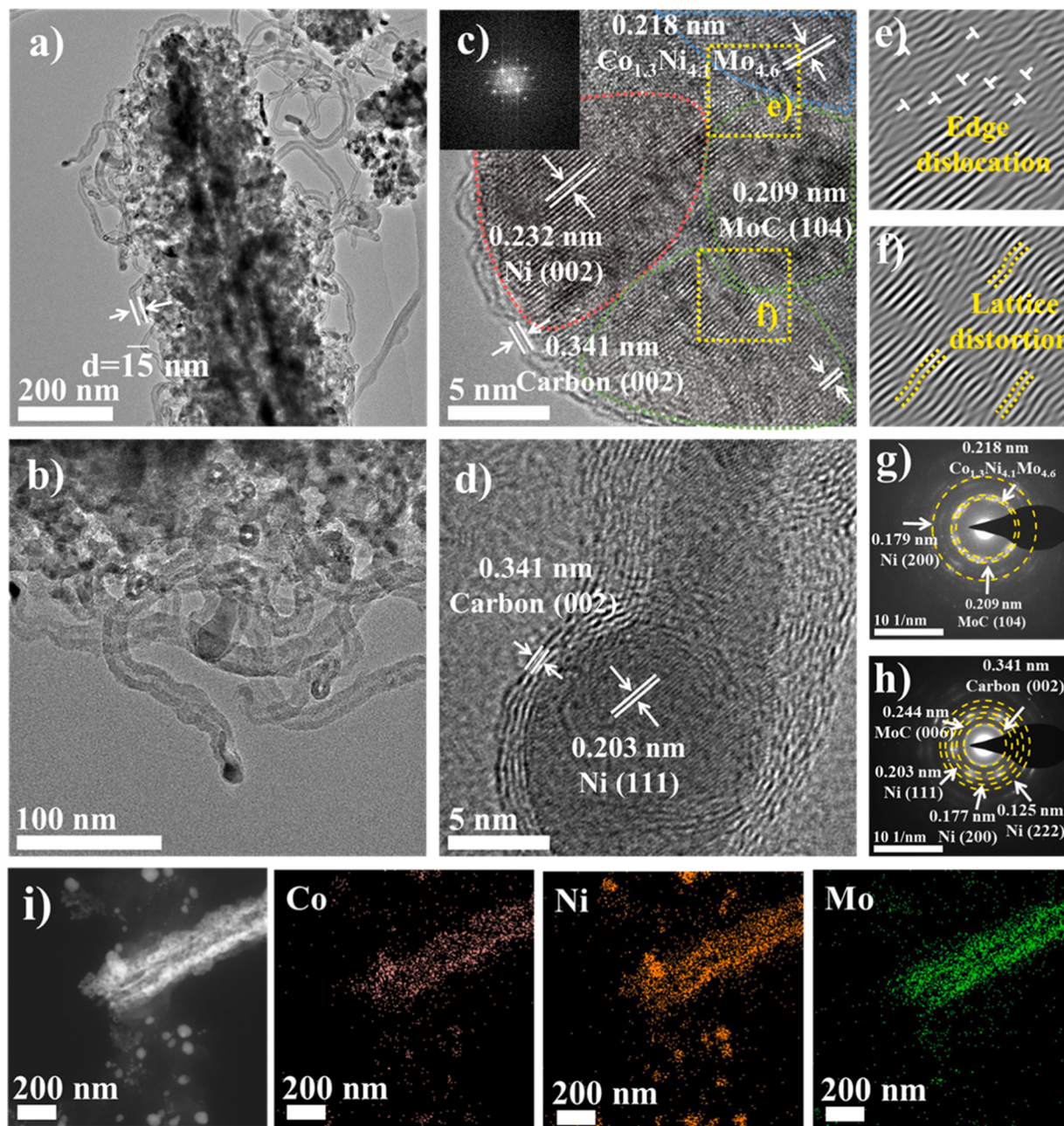


Fig. 3. (a-d) TEM images with corresponding FFT patterns (c inset), (e, f) corresponding FFT and inverse FFT of the selected area in (c), (g, h) corresponding SAED patterns and (i) high-resolution elemental mappings of CNT/MoC/NMC-3 composite.

carbon layers can promote the OH^- adsorption and OER process [35]. The lowest Tafel slope of $58.71 \text{ mV dec}^{-1}$ for CNT/MoC/NMC-3 verifies the highest OER reaction kinetics (Fig. 4e).

To further estimate the mass transfer kinetics, the electrochemical impedance spectroscopy (EIS) is measured and fitted by equivalent circuit (Fig. 4c, f). The values of the solution resistance (R_s), interface resistance (R_p), and charge-transfer resistance (R_{ct}) of CNT/MoC/NMC-3 composite are the smallest among all electrodes, which are 2.19, 0.21, and 1.12Ω for HER, and 2.26, 0.83, and 4.81Ω for OER, respectively (Tables S2 and S3). This result demonstrates the promotion of the mass transfer efficiency by the extension of the encapsulated Ni along with CNTs into the electrolyte and the synergistic effect between multiple dominant components. Additionally, the turnover frequency (TOF) values of the CNT/MoC/NMC-3 are calculated to be 0.699 s^{-1} for HER and 0.937 s^{-1} for OER (Fig. 4h, S11), respectively, indicating the

superior instantaneous efficiency for water electrolysis. Furthermore, the CNT/MoC/NMC-3 also reveals excellent stability within 40 h long-term catalysis at 100 mA cm^{-2} for both HER and OER (Fig. S12). As summarized in Fig. 4i, the theoretical overall overpotentials indicate the lowest overpotential of the CNT/MoC/NMC-3 hybrid (277 mV), suggesting the excellent overall water splitting efficiency of the bifunctional catalyst. Moreover, the two-electrode electrolyzer is assembled by employing CNT/MoC/NMC-3 as both anode and cathode, a low cell voltage of 1.51 V is required to achieve 10 mA cm^{-2} (Fig. S13a, b), which is superior than most of the high-end devices (Fig. S14). In addition, the effects of different growth temperatures and carbon sources (methane, melamine, and dicyandiamide) on the morphology and electrocatalytic properties during the CNTs growth process are also investigated, while the results demonstrate the optimal treatment temperature of 600°C (Figs. S15–S19, Tables S4 and S5), and acetylene is

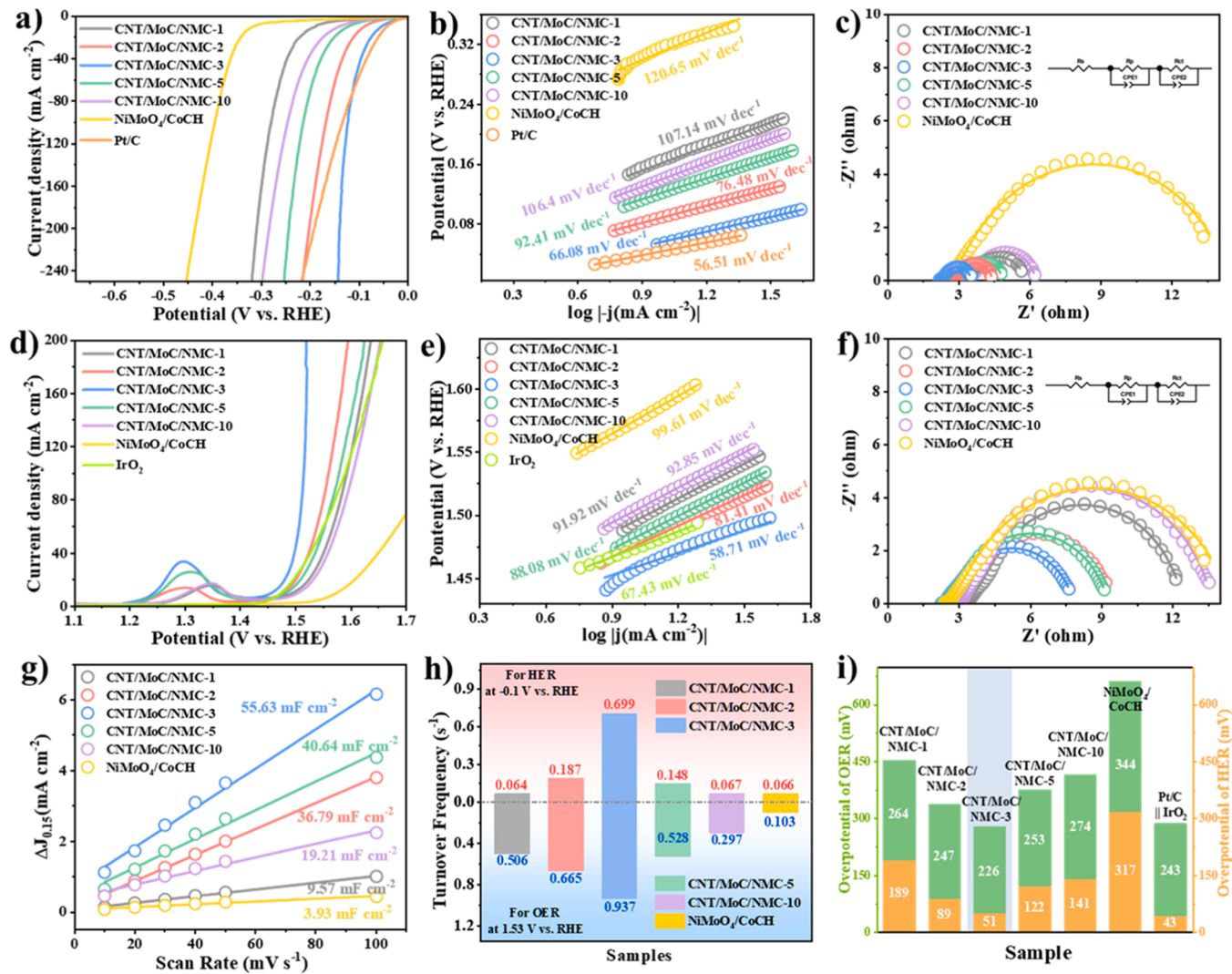


Fig. 4. (a) LSV curves, (b) Tafel plots, (c) Nyquist plots for HER; (d) LSV curves, (e) Tafel plots, (f) Nyquist plots for OER; (g) C_{dl} values and (h) TOF values of the CNT/MoC/NMC-x and NiMoO₄/CoCH electrodes; (i) The overall overpotential of the corresponding electrodes obtained at 10 mA cm⁻².

selected as the best-matched carbon source (Figs. S20–23). The relatively low growth temperature and optimal carbon source are beneficial to maintain the hierarchical nanostructure as well as increase the preparation economy.

3.2.2. UOR and urea electrolysis

In order to decrease the operation potential during H₂ generation, the UOR reaction is further studied to substitute OER process. In three-electrode configuration, the LSV curve of the CNT/MoC/NMC-3 reveals enhanced UOR activity with potential of 1.257 V at 10 mA cm⁻² (Fig. 5a), which is much lower than that of the OER. In addition, varied urea concentrations are investigated, while 0.5 M is demonstrated to be the most appropriate concentration for this system (Fig. S24). Moreover, the oxidation peak position of OER is in line with that of the UOR (Fig. S25), confirming that the encapsulated Ni species are conducive to generate NiOOH and serve as active species for anodic oxidation reaction. In comparison, the NiMoO₄/CoCH and IrO₂ electrodes reveal no improvement in UOR activity (1.576 V and 1.484 V at 10 mA cm⁻²). Furthermore, the CNT/MoC/NMC-3 exhibits Tafel slope of 55.4 mV dec⁻¹, which is considerably lower than 134.4 mV dec⁻¹ for IrO₂ electrode, indicating the optimal adsorption characteristics and rapid reaction kinetics for the urea molecules (Fig. 5b). The boost UOR activity of the CNT/MoC/NMC-3 can also be proven by the highest C_{dl} value (65.8 mV cm⁻², Fig. 5c, S26), the lowest interface resistance and fastest

charge-transfer kinetics (0.41 Ω of R_{p} and 3.06 Ω of R_{ct} , Fig. 5d, Table S6), and the superior intrinsic electrocatalytic activity (TOF value of 1.710 s⁻¹, Fig. S27). Furthermore, with the absence of CNTs arrays and MoC active substances, both composites reveal inferior electrocatalytic behavior compared with CNT/MoC/NMC-3 (Figs. S28–S34, Tables S7 and S8), verifying the enormous benefits of reasonable structural design and integrated coupling between multiple active components.

To investigate the potential practical application, the CNT/MoC/NMC-3 electrode is assembled to the urea electrolyzer. The LSV curve for HER in urea-containing solution only exhibits a slightly cathodic shift compared with that in pure KOH, suggesting a robust electrocatalytic ability under various conditions (Fig. S35). The theoretical cell voltage of the device at 10 mA cm⁻² is 1.290 V in urea-containing electrolyte, which is 0.22 V lower than that in water electrolysis, indicating an enhanced H₂ production efficiency (Fig. 5e). Specifically, the actual measured cell voltage is 1.291 V (Fig. 5f), which is close to theoretical value and is comparable or better than most of the high-end electrocatalysts (Fig. 5h, Table S9). In addition, the electrolyzer can react steadily under varied constant cell voltage from 1.3 V to 1.7 V for 24 h (Fig. 5g and Fig. S36), while the enlarged current density disparities between urea electrocatalysis and water splitting can be observed with increasing bias voltage, suggesting excellent operation durability and activity. Moreover, the parallel aligned structure with plenty CNTs

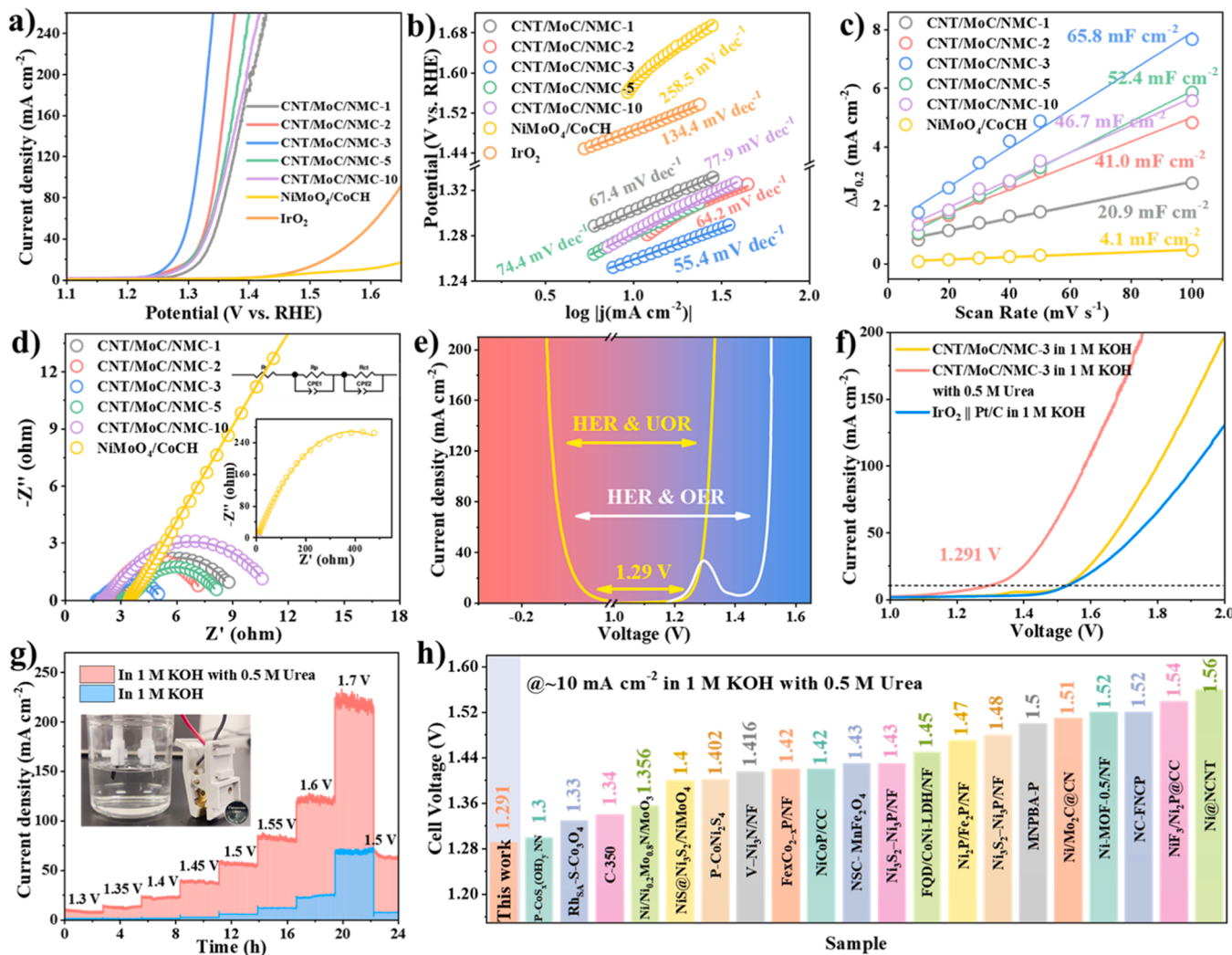


Fig. 5. (a) LSV curves, (b) Tafel plots, (c) C_{dl} values, and (d) Nyquist plots of CNT/MoC/NMC- x , NiMoO₄/CoCH, and IrO₂ electrodes for UOR. (e) Theoretical voltage values of CNT/MoC/NMC-3 toward HER with UOR/OER. (f) LSV curves of CNT/MoC/NMC-3 and Pt/C||IrO₂ systems in various electrolytes. (g) Durability of electrolyzer at various cell voltage, inset: electrolyzer powered by 1.5 V button battery. (h) Comparison of cell voltage required to drive 10 mA cm⁻² of various urea electrolysis catalysts.

remains unchanged under fast surface reaction and bubble disturbance (Fig. S37), verifying the robust structural stability. Considering the portable advantage of devices powered by commercial batteries, the urea electrolysis configuration can be driven by single 1.5 V button battery (Fig. 5g, Video S3). Profiting from the coupling of intrinsic activity and structural superiority between multi-component, urea electrolysis occurs violently and the generated bubbles can be released under guidance of CNTs arrays.

3.3. Mechanism analysis of enhanced electrochemical activities

3.3.1. The evolution of electronic structure

To understand the evolution of electronic structure and active intermediates under the applied potential, related ex-situ and in-situ characterizations are performed. The surface valence states of CNT/MoC/NMC-3 before/after UOR is investigated by X-ray photoelectron spectroscopy (XPS, Fig. S38). All the binding energies of metal elements reveal obvious positive shift after long-term UOR operation, reflecting the promotion of corresponding oxidation states. In Ni 2p spectra, the strong peaks located at 853.1 eV and 870.2 eV can be assigned to Ni⁰ species (Fig. 6a) [36], which is consistent with massive metallic Ni nanoparticles inside CNTs and on the tri-metallic alloy surface. The

weak peaks centered at 855.6 eV and 873.0 eV belongs to the partially oxidized Ni²⁺ species. After urea electrolysis, a pair of new peaks appear at 857.5 eV and 875.6 eV, which are attributed to Ni³⁺ [37], while the peaks for metallic Ni disappear. Moreover, the Mo species are completely converted to Mo⁶⁺ under the long-period oxidation conditions (Fig. 6b). In Co 2p spectra, the Co⁰ signal also disappears after UOR (Fig. 6c), while the proportion of Co³⁺ content increases from 21.26% to 56.38%. The significant elevation of the oxidation state of CNT/MoC/NMC-3 after UOR can also be confirmed by XRD and Raman results (Fig. S39).

For O 1s, four peaks located at 530.3, 531.2, 532.1, and 533.4 eV are related to the metal-oxygen, hydroxyl species, oxygen vacancies, and absorbed oxygen, respectively (Fig. 6d) [38]. The increased O-H content and the appearance of Ni³⁺ further imply the formation of nickel oxy-hydroxide [39]. The N 1s in Fig. 6e corresponds to the presence of pyridinic N (398.4 eV), pyrrolic N (400.2 eV), and graphitic N (401.8 eV) [35]. The peak located at 394.3 eV is attributed to the Mo 3p [1], where N-Ni/Mo (396.9 eV) [40] is detected due to the bonding of Ni/Mo species with N atoms. The N 1s signal is enhanced significantly after continuous electrolysis, probably resulting from the adsorption and transformation of nitrogen-containing intermediates during UOR process. The accumulation of pyridinic/graphitic N electron-acceptor

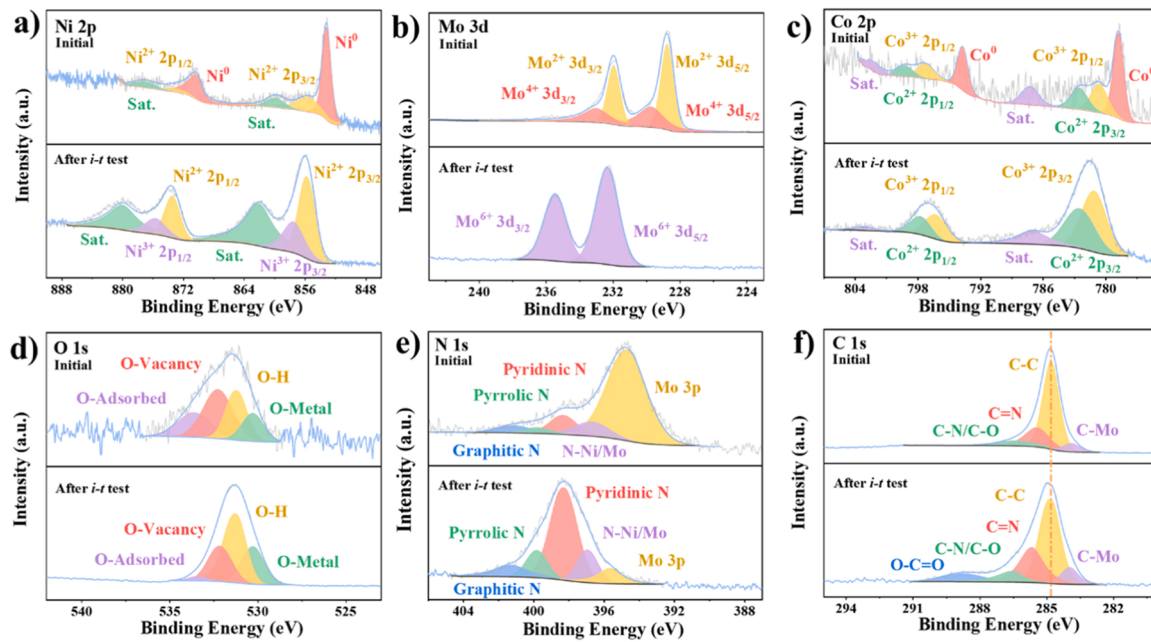


Fig. 6. XPS (a) Ni 2p, (b) Mo 3d, (c) Co 2p, (d) O 1s, (e) N 1s, (f) C 1s spectra of the CNT/MoC/NMC-3 before/after long-term UOR.

potentially generates positive charges on adjacent sp^2 -hybridized carbon atoms, thus accelerate the intrinsic reaction kinetics [41]. The binding energies of C 1s at 283.9, 284.8, 285.4, and 286.3 eV are in accordance with the C-Mo, C-C, C=N, and C-N/C-O (Fig. 6f) [42]. Identification of C-N and C=N bonds confirms the entrance of N atoms into the carbon skeleton and stimulates chemical interactions with adjacent metal/carbon atoms, which can generate structural defects in CNTs to generate activated chemisorption sites [35]. After urea electrolysis, the appearance of the O-C=O bond located at 289.3 eV attaches to the interaction of carbonate anions in electrolyte into the carbon interlayer [43].

3.3.2. The evolution of active intermediates

To further identify the surface states of multi-components heterostructure, in-situ Raman spectroscopy is employed to clarify the real-time intermediates evolution of CNT/MoC/NMC-3 electrode. The varied applied potentials are compensated by solution resistance to eliminate the influence of different device configuration (Fig. S40). Moreover, with the addition of electrolyte, a peak belonging to the O-H stretching of water appears at 1639 cm^{-1} (Fig. S41). For HER, two peaks around 319 cm^{-1} and 895 cm^{-1} emerge at 0.873 V (vs. RHE, Fig. 7a, b), indicating the transformation of low-valent Mo species to $\text{Mo}^{6+}\text{-O}$ in the multi-component catalysts after activation [44]. With increasing negative potentials, a gradual weakening of peak signals is observed until hydrogen evolution occurs entirely at -0.027 V . The dynamic evolving behavior of Mo component at reductive potentials is revealed by the coordination of hexagonal MoC with CoNiMo alloy during HER (more details are provided in DFT calculations below). In comparison, the $\text{NiMoO}_4/\text{CoCH}$ precursor reveals three peaks, the two located at 339 cm^{-1} and 838 cm^{-1} belong to MoO_4^{2-} vibrations, while the sharp peak at 927 cm^{-1} can be assigned to symmetric stretching of Ni-O-Mo (Fig. S42) [45,46]. These peaks are significantly strengthened with the increase of applied potential, suggesting the HER reaction occurs at intrinsically inert NiMoO_4 sites due to the relatively negative Gibbs free energies of H^* [47]. Thus, the optimized electronic structure can balance hydrogen adsorption/desorption and lead to synergistically-enhanced HER kinetics [48,49]. In addition, the surface evolution of CNT/MoC/NMC-3 for HER in urea-alkaline electrolyte is also explored, though some of the signals are influenced by the urea, the variation trend is consistent with the activity mechanism in pure KOH

electrolyte (Fig. S43).

For UOR process, a peak appears at 1001 cm^{-1} when no bias voltage is applied (Fig. 7c, d), which is attributed to symmetric C-N stretch of urea molecules attached onto carbon surface [50]. Besides, the peak at 1092 cm^{-1} is assigned to the symmetric stretch of CO_3^{2-} , which is one of the products in UOR [51]. A pair of D and G peaks can be noticed, which may due to synergistically enhancement of urea molecules to graphite carbon (Fig. S43). The D and G bands disappear when the applied potential reaches 1.353 V , and is reversible after CV cycling (Fig. S44). The doublet peaks of $\gamma\text{-NiOOH}$ located at 475 cm^{-1} and 550 cm^{-1} emerge at 1.353 V [52], indicating the partial reconstruction of massive metallic Ni particles inside carbon layers. Besides, a diffraction peak attributed to NiC_x can be detected in the post-electrolysis XRD pattern (Fig. S39a), verifying the long-term continuous mass transfer of the activated Ni particles to the electrolyte during UOR. In addition, transient evolution of the $\gamma\text{-NiOOH}$ intermediate can also be observed in OER process of CNT/MoC/NMC-3 (Fig. S45). The activation of Ni nanoparticles during anodic oxidation can also be demonstrated by evolving potential of Ni-based intermediates, corresponding to the clear redox peaks in CV curve due to the Faraday process of Ni (III) conversion (Fig. 7e). The relatively high degradation of catalytic performance in near-neutral electrolyte also confirms that these electrocatalytic active components with positive charges can favorable the surface OH^- adsorption kinetics to boost the reaction (Fig. S46). In comparison, the in-situ Raman of $\text{NiMoO}_4/\text{CoCH}$ in UOR reveals the absence of Ni-based intermediates (Fig. S47), the insufficient active sites produced by NiMoO_4 may directly consumed by urea [53]. Moreover, due to the chemisorption of OH radicals in alkali electrolyte, a pair of peaks located at 461 cm^{-1} and 528 cm^{-1} appear (Fig. S48) [54], which belongs to $\text{Ni}(\text{OH})_2$ and cannot be transformed into $\gamma\text{-NiOOH}$. It is verified that the monoclinic nickel molybdate oxides exhibit limited activity and sluggish reaction kinetics in UOR than in OER (Fig. S49).

Furthermore, DFT calculations are carried out to investigate the mutual coupling and evolution process of active components, specifically CoNiMo and MoC, and the appropriate theoretical models are constructed. Among the three typical geometries of CoNiMo alloy, namely, Mo-bulk-rich, Mo-surf.-rich, and Mo-averaged surfaces, our findings indicate that the Mo-surf.-rich CoNiMo alloy surface exhibits highest thermodynamic stability, with an energy difference of at least 1.1 eV lower than the other systems (Fig. 8a). This particular surface

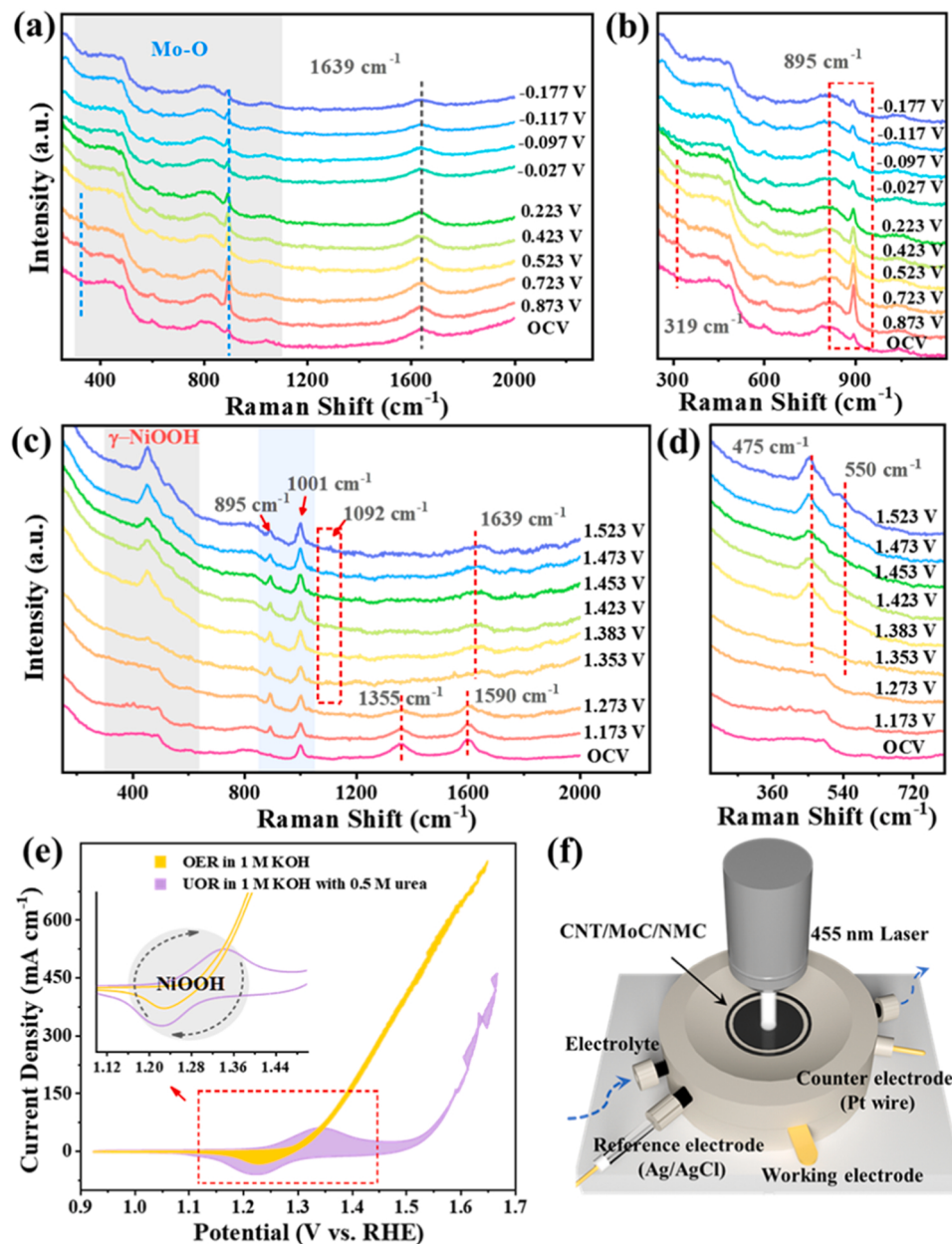


Fig. 7. *In-situ* Raman spectra of the CNT/MoC/NMC-3 as a function of applied potential vs. RHE in (a, b) HER and (c, d) UOR. (e) CV curves of the CNT/MoC/NMC-3 at 5 mV s⁻¹. (f) Schematic illustration of the *in-situ* Raman cell.

undergoes noticeable surface reconstruction, evidenced by the formation of atom steps, while still maintaining a hexagonal shape with dense packing (Fig. 8b). The reconstruction of the Mo-surf.-rich surface is attributed to the larger radius of Mo (145 pm) compared to Ni and Co (135 pm), which relieves the stress/strain present in the other systems and contributes to its enhanced thermodynamic stability. Moreover, the most stable surfaces among the Mo-bulk-rich, Mo-surf.-rich, and Mo-averaged surface-series are tested as the active sites for the hydrogen evolution reaction. The results, depicted in Fig. 8c, clearly demonstrate that the Mo-surf.-rich surface enables the Heyrovsky step (${}^*H + H_2O + e^- \rightarrow OH^- + {}^*H_2$) without requiring negative potentials. Conversely, minimum applied potentials of -0.31 V and -0.54 V are necessary for the Mo-averaged surface and Mo-bulk-rich surface, respectively. It is important to note that the Volmer step of $2 H \rightarrow {}^*H_2$ cannot occur on CoNiMo alloy surfaces. Therefore, we propose that the Mo-surf.-rich surface represents the super-active site for HER process (Fig. 8d). Regarding the HER on MoC, a negative potential of -0.50 V is required

to facilitate the reaction (Fig. S50).

Therefore, the excellent electrocatalytic performance in HER, OER, and UOR of the CNT/MoC/NMC-3 electrode can be attributed to the following reasons: (1) The parallel nanosheet arrays with densely coated CNTs can significantly enlarge the accessible active area and reduce the steric hindrance of active sites, while the out-plane CNTs arrays can also guide the bubble desorption. (2) *In-situ* growth on NiMoO₄ surface without extra-seeds addition can regulate the morphology of CNTs, together with remarkable activity and stability of the embedded ultra-small Ni nanoparticles under carbon layers protection. (3) The intermediate evolution process in multi-interfacial heterostructures can facilitate the electrocatalytic activity: the coordination of MoC and CoNiMo alloys induce the migration of Mo species to outer surface under negative potentials, resulting in thermodynamically stable Mo-surf.-rich surface preferable for HER; while plenty of metallic Ni nanoparticles wrapped inside carbon layers can evolve into highly active γ -NiOOH sites for OER and UOR. By design the multi-component integrated

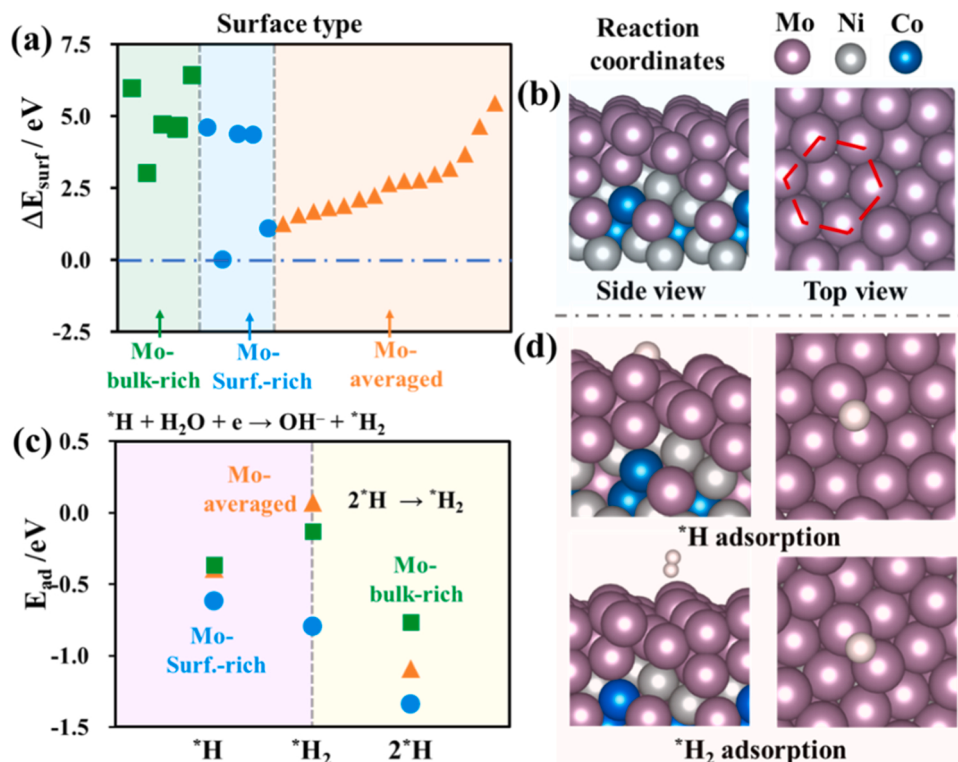


Fig. 8. CoNiMo as the active sites for HER. (a) The energy difference of the three typical surface series. (b) The side and top view of the reconstructed Mo-surf.-rich surface. (c) The energy diagram of the Herovský step and Volmer step in HER. (d) Adsorption geometries of ${}^* \text{H}$ and ${}^* \text{H}_2$.

heterostructures, it may provide novel idea for the development of industrial hydrogen production in the future.

4. Conclusions

In summary, we report a facile strategy for in-situ construction of integrated hierarchical tri-functional CNTs/MoC/CoNiMo heterostructures, and elucidate the dynamic evolution of multiple components during electrocatalysis. The nickel nanoparticles protected by carbon layers possess superior activity and stability, which can accelerate the formation of γ -NiOOH active intermediates for OER/UOR. The MoC cooperates with CoNiMo tri-metals can form Mo-surf.-rich surface to strengthen intrinsic activity for HER. Driven by the structural advantages of out-plane extended CNTs and parallel aligned nanosheets, bubbles separation and active intermediate evolution are promoted, ultimately remarkably accelerating the electrocatalytic reaction. Therefore, the optimized CNT/MoC/NMC-3 can achieve low overpotentials of 51 mV and 226 mV at 10 mA cm^{-2} for HER and OER, as well as an exceptional potential of 1.257 V to deliver 10 mA cm^{-2} for UOR. Furthermore, the assembled symmetric electrolyzer can achieve low cell voltage of 1.291 V at 10 mA cm^{-2} for urea electrolysis. This paper integrates the fabrication of high-efficiency catalyst and the optimization of electrolysis system, which offers a promising pathway for achieving hydrogen economy coupled with purification of urea-rich wastewater.

Supporting information

Supplementary experimental section, electrochemical tests and related calculation, fitted equivalent circuits, and SEM, EDS, XRD, XPS, Raman tests of the composites are listed in the [Supporting Information](#).

CRedit authorship contribution statement

X. L.: Investigation, Experimental, Data analysis, Writing – original draft. **K. D.**: Data analysis. **P. L.**: Data analysis, Visualization. **X. L.**: Data analysis. **W. T.**: Visualization, Investigation. **K. M.**: Visualization, Writing – review & editing. **H. L.**: Theoretical simulation. **J. J.**: Conceptualization, Investigation, Supervision, Writing – review & editing, Funding acquisition.

Declaration of Competing Interest

The authors declare that they have no known competing financial interests or personal relationships that could have appeared to influence the work reported in this paper.

Data Availability

Data will be made available on request.

Acknowledgements

The authors acknowledge support from National Natural Science Foundation of China (21978178, 22278282), Sichuan Science and Technology Program (2023NSFSC1915). We would like to thank Yanping Huang and Jie Wei from Center of Engineering Experimental Teaching for SEM and Raman capturing, and Yingming Zhu from the Institute of New Energy and Low Carbon Technology for XRD analysis.

Appendix A. Supporting information

Supplementary data associated with this article can be found in the online version at [doi:10.1016/j.apcatb.2023.123470](https://doi.org/10.1016/j.apcatb.2023.123470).

References

[1] L. Yu, Q. Zhu, S. Song, B. McElhenny, D. Wang, C. Wu, Z. Qin, J. Bao, Y. Yu, S. Chen, Z. Ren, Non-noble metal-nitride based electrocatalysts for high-performance alkaline seawater electrolysis, *Nat. Commun.* 10 (2019) 5106.

[2] Y.K. Chen, J.Y. Yu, J. Jia, F. Liu, Y.W. Zhang, G.W. Xiong, R.T. Zhang, R.Q. Yang, D.H. Sun, H. Liu, W.J. Zhou, Metallic Ni₃Mo₃N porous microrods with abundant catalytic sites as efficient electrocatalyst for large current density and superstability of hydrogen evolution reaction and water splitting, *Appl. Catal. B Environ.* 272 (2020), 118956.

[3] F. Gao, J. He, H. Wang, J. Lin, R. Chen, K. Yi, F. Huang, Z. Lin, M. Wang, Te-mediated electro-driven oxygen evolution reaction, *Nano Res. Energy* 1 (2022) 9120029.

[4] Q. Zhang, K. Lian, Q. Liu, G. Qi, S. Zhang, J. Luo, X. Liu, High entropy alloy nanoparticles as efficient catalysts for alkaline overall seawater splitting and Zn-air batteries, *J. Colloid Interface Sci.* 646 (2023) 844–854.

[5] J. Wang, C.-X. Zhao, J.-N. Liu, D. Ren, B.-Q. Li, J.-Q. Huang, Q. Zhang, Quantitative kinetic analysis on oxygen reduction reaction: a perspective, *Nano Mater. Sci.* 3 (2021) 313–318.

[6] Z. Wu, P. Yang, Q. Li, W. Xiao, Z. Li, G. Xu, F. Liu, B. Jia, T. Ma, S. Feng, L. Wang, Microwave synthesis of Pt clusters on black TiO₂ with abundant oxygen vacancies for efficient acidic electrocatalytic hydrogen evolution, *Angew. Chem. Int. Ed.* 62 (2023), e202300406.

[7] Z. Wu, Y. Gao, Z. Wang, W. Xiao, X. Wang, B. Li, Z. Li, X. Liu, T. Ma, L. Wang, Surface-enriched ultrafine Pt nanoparticles coupled with defective CoP as efficient trifunctional electrocatalyst for overall water splitting and flexible Zn-air battery, *Chin. J. Catal.* 46 (2023) 36–47.

[8] H. Wang, P. Yang, X. Sun, W. Xiao, X. Wang, M. Tian, G. Xu, Z. Li, Y. Zhang, F. Liu, L. Wang, Z. Wu, Co-Ru alloy nanoparticles decorated onto two-dimensional nitrogen-doped carbon nanosheets towards hydrogen/oxygen evolution reaction and oxygen reduction reaction, *J. Energy Chem.* 87 (2023) 286–294.

[9] Q. Li, X. Luan, Z. Xiao, W. Xiao, G. Xu, Z. Li, Z. Wu, L. Wang, Ultrafast microwave synthesis of Ru-doped MoP with abundant P vacancies as the electrocatalyst for hydrogen generation in a wide pH range, *Inorg. Chem.* 62 (2023) 9687–9694.

[10] Z. Chen, Q. Li, H. Xiang, Y. Wang, P. Yang, C. Dai, H. Zhang, W. Xiao, Z. Wu, L. Wang, Hierarchical porous NiFe-P@NC as an efficient electrocatalyst for alkaline hydrogen production and seawater electrolysis at high current density, *Inorg. Chem. Front.* 10 (2023) 1493–1500.

[11] L.Q. Deng, K. Zhang, D. Shi, S.F. Liu, D.Q. Xu, Y.L. Shao, J.X. Shen, Y.Z. Wu, X. P. Hao, Rational design of Schottky heterojunction with modulating surface electron density for high-performance overall water splitting, *Appl. Catal. B Environ.* 299 (2021), 120660.

[12] Z. Wu, D. Nie, M. Song, T. Jiao, G. Fu, X. Liu, Facile synthesis of Co-Fe-B-P nanochains as an efficient bifunctional electrocatalyst for overall water-splitting, *Nanoscale* 11 (2019) 7506–7512.

[13] L. Wu, F. Zhang, S. Song, M. Ning, Q. Zhu, J. Zhou, G. Gao, Z. Chen, Q. Zhou, X. Xing, T. Tong, Y. Yao, J. Bao, L. Yu, S. Chen, Z. Ren, Efficient alkaline water/seawater hydrogen evolution by a nanorod-nanoparticle-structured Ni-MoN catalyst with fast water-dissociation kinetics, *Adv. Mater.* 34 (2022), e2201774.

[14] Z. Yu, C. Liu, J. Chen, Z. Yuan, Y. Chen, L. Wei, High-performance Fe-N-C electrocatalysts with a “chain mail” protective shield, *Nano Mater. Sci.* 3 (2021) 420–428.

[15] Z.X. Xu, S. Jin, M.H. Seo, X.L. Wang, Hierarchical Ni-Mo₂C/N-doped carbon Mott-Schottky array for water electrolysis, *Appl. Catal. B Environ.* 292 (2021), 120168.

[16] Q. Zhang, W. Xiao, W.H. Guo, Y.X. Yang, J.L. Lei, H.Q. Luo, N.B. Li, Macroporous array induced multiscale modulation at the surface/interface of Co(OH)₂/NiMo self-supporting electrode for effective overall water splitting, *Adv. Funct. Mater.* 31 (2021) 2102117.

[17] X. Peng, Y. Mi, X. Liu, J. Sun, Y. Qiu, S. Zhang, X. Ke, X. Wang, J. Luo, Self-driven dual hydrogen production system based on a bifunctional single-atomic Rh catalyst, *J. Mater. Chem. A* 10 (2022) 6134–6145.

[18] C. Cao, D.D. Ma, J. Jia, Q. Xu, X.T. Wu, Q.L. Zhu, Divergent paths, same goal: a pair-electrosynthesis tactic for cost-efficient and exclusive formate production by metal-organic-framework-derived 2D electrocatalysts, *Adv. Mater.* 33 (2021), e2008631.

[19] M. Song, Z. Zhang, Q. Li, W. Jin, Z. Wu, G. Fu, X. Liu, Ni-foam supported Co(OH)F and Co-P nanoarrays for energy-efficient hydrogen production via urea electrolysis, *J. Mater. Chem. A* 7 (2019) 3697–3703.

[20] H. Shen, T. Wei, Q. Liu, S. Zhang, J. Luo, X. Liu, Heterogeneous Ni-MoN nanosheet-assembled microspheres for urea-assisted hydrogen production, *J. Colloid Interface Sci.* 634 (2023) 730–736.

[21] Q. Liu, X.B. Liao, Y.H. Tang, J.H. Wang, X.Z. Lv, X.L. Pan, R.H. Lu, Y. Zhao, X.Y. Yu, H.B. Wu, Low-coordinated cobalt arrays for efficient hydrazine electrooxidation, *Energ. Environ. Sci.* 15 (2022) 3246–3256.

[22] L. Guo, J. Chi, J. Zhu, T. Cui, J. Lai, L. Wang, Dual-doping NiMoO₄ with multi-channel structure enable urea-assisted energy-saving H₂ production at large current density in alkaline seawater, *Appl. Catal. B Environ.* 320 (2023), 121977.

[23] T. Wei, G. Meng, Y. Zhou, Z. Wang, Q. Liu, J. Luo, X. Liu, Amorphous Fe-Co oxide as an active and durable bifunctional catalyst for the urea-assisted H₂ evolution reaction in seawater, *Chem. Commun.* 59 (2023) 9992–9995.

[24] A. Kumar, X.H. Liu, J. Lee, B. Debnath, A.R. Jadhav, X.D. Shao, V.Q. Bui, Y. Hwang, Y. Liu, M.G. Kim, H. Lee, Discovering ultrahigh loading of single-metal-atoms via surface tensile-strain for unprecedented urea electrolysis, *Energy Environ. Sci.* 14 (2021) 6494–6505.

[25] X. Jia, H. Kang, X. Yang, Y. Li, K. Cui, X. Wu, W. Qin, G. Wu, Amorphous Ni(III)-based sulfides as bifunctional water and urea oxidation anode electrocatalysts for hydrogen generation from urea-containing water, *Appl. Catal. B Environ.* 312 (2022), 121389.

[26] X. Liu, P. Liu, F. Wang, X. Lv, T. Yang, W. Tian, C. Wang, S. Tan, J. Ji, Plasma-induced defect engineering and cation refilling of NiMoO₄ parallel arrays for overall water splitting, *ACS Appl. Mater. Interfaces* 13 (2021) 41545–41554.

[27] F.F. Wang, K. Ma, W. Tian, J.C. Dong, H. Han, H.P. Wang, K. Deng, H.R. Yue, Y. X. Zhang, W. Jiang, J.Y. Ji, P-doped NiMoO₄ parallel arrays anchored on cobalt carbonate hydroxide with oxygen vacancies and mass transfer channels for supercapacitors and oxygen evolution, *J. Mater. Chem. A* 7 (2019) 19589–19596.

[28] D.D. Li, F. Xu, X. Tang, S. Dai, T.C. Pu, X.L. Liu, P.F. Tian, F.Z. Xuan, Z. Xu, I. E. Wachs, M.H. Zhu, Induced activation of the commercial Cu/ZnO/Al₂O₃ catalyst for the steam reforming of methanol, *Nat. Catal.* 5 (2022) 99–108.

[29] Y. Wu, Y. Zhao, P. Zhai, C. Wang, J. Gao, L. Sun, J. Hou, Triggering lattice oxygen activation of single-atomic Mo sites anchored on Ni-Fe oxyhydroxides nanoarrays for electrochemical water oxidation, *Adv. Mater.* (2022), e2202523.

[30] Y.Q. Lei, T.T. Xu, S.H. Ye, L.R. Zheng, P. Liao, W. Xiong, J. Hu, Y.J. Wang, J. P. Wang, X.Z. Ren, C.X. He, Q.L. Zhang, J.H. Liu, X.L. Sun, Engineering defect-rich Fe-doped NiO coupled Ni cluster nanotube arrays with excellent oxygen evolution activity, *Appl. Catal. B Environ.* 285 (2021), 119809.

[31] Y. Ma, M. Chen, H. Geng, H. Dong, P. Wu, X. Li, G. Guan, T. Wang, Synergistically tuning electronic structure of porous μ -Mo₂C spheres by Co doping and Mo-vacancies defect engineering for optimizing hydrogen evolution reaction activity, *Adv. Funct. Mater.* 30 (2020) 2000561.

[32] M. Xiong, Z. Gao, Y. Qin, Spillover in heterogeneous catalysis: new insights and opportunities, *ACS Catal.* 11 (2021) 3159–3172.

[33] M. Tan, Y. Yang, Y. Yang, J. Chen, Z. Zhang, G. Fu, J. Lin, S. Wan, S. Wang, Y. Wang, Hydrogen spillover assisted by oxygenate molecules over nonreducible oxides, *Nat. Commun.* 13 (2022) 1457.

[34] J.X. Kang, X.Y. Qiu, Q. Hu, J. Zhong, X. Gao, R. Huang, C.Z. Wan, L.M. Liu, X. F. Duan, L. Guo, Valence oscillation and dynamic active sites in monolayer NiCo hydroxides for water oxidation, *Nat. Catal.* 4 (2021) 1050–1058.

[35] L. Yan, Y. Xu, P. Chen, S. Zhang, H. Jiang, L. Yang, Y. Wang, L. Zhang, J. Shen, X. Zhao, L. Wang, A freestanding 3D heterostructure film stitched by MOF-derived carbon nanotube microsphere superstructure and reduced graphene oxide sheets: a superior multifunctional electrode for overall water splitting and Zn-air batteries, *Adv. Mater.* 32 (2020), e2003313.

[36] A. Salah, L.N. Zhang, H.Q. Tan, F.Y. Yu, Z.L. Lang, N. Al-Ansi, Y.G. Li, Advanced Ru/Ni/WC@NPC multi-interfacial electrocatalyst for efficient sustainable hydrogen and chlor-alkali Co-production, *Adv. Energy Mater.* 12 (2022) 2200332.

[37] B. Mondal, N. Karjule, C. Singh, R. Shimoni, M. Volokh, I. Hod, M. Shalom, Unraveling the mechanisms of electrocatalytic oxygenation and dehydrogenation of organic molecules to value-added chemicals over a Ni-Fe oxide catalyst, *Adv. Energy Mater.* 11 (2021) 2101858.

[38] R. Li, B. Hu, T. Yu, H. Chen, Y. Wang, S. Song, Insights into correlation among surface-structure-activity of cobalt-derived pre-catalyst for oxygen evolution reaction, *Adv. Sci.* 7 (2020) 1902830.

[39] Y. Huang, S.L. Zhang, X.F. Lu, Z.P. Wu, D. Luan, X.W.D. Lou, Trimetallic spinel Ni_{Co_{2-x}}Fe_xO₄ nanoboxes for highly efficient electrocatalytic oxygen evolution, *Angew. Chem. Int. Ed.* 60 (2021) 11841–11846.

[40] C.Q. Huang, L. Yu, W. Zhang, Q. Xiao, J.Q. Zhou, Y.L. Zhang, P.F. An, J. Zhang, Y. Yu, N-Doped Ni-Mo based sulfides for high-efficiency and stable hydrogen evolution reaction, *Appl. Catal. B Environ.* 276 (2020), 119137.

[41] Q. Lu, J. Yu, X.H. Zou, K.M. Liao, P. Tan, W. Zhou, M. Ni, Z.P. Shao, Self-catalyzed growth of Co, N-codoped CNTs on carbon-encased Co₃S₄ surface: a noble-metal-free bifunctional oxygen electrocatalyst for flexible solid Zn-air batteries, *Adv. Funct. Mater.* 29 (2019) 1904481.

[42] H. Yan, Y. Xie, Y. Jiao, A. Wu, C. Tian, X. Zhang, L. Wang, H. Fu, Holey reduced graphene oxide coupled with an Mo₂N-Mo₂C heterojunction for efficient hydrogen evolution, *Adv. Mater.* 30 (2018) 1704156.

[43] Y.L. Li, B.M. Jia, Y.Z. Fan, K.L. Zhu, G.Q. Li, C.Y. Su, Bimetallic zeolitic imidazolite framework derived carbon nanotubes embedded with Co nanoparticles for efficient bifunctional oxygen electrocatalyst, *Adv. Energy Mater.* 8 (2018) 1702048.

[44] J. Choi, D. Kim, W.R. Zheng, B.Y. Yan, Y. Li, L.Y.S. Lee, Y. Piao, Interface engineered NiFe₂O_{4-x}/NiMoO₄ nanowire arrays for electrochemical oxygen evolution, *Appl. Catal. B Environ.* 286 (2021), 119857.

[45] G. Solomon, A. Landstrom, R. Mazzaro, M. Jugovac, P. Moras, E. Cattaruzza, V. Morandi, I. Concina, A. Vomiero, NiMoO₄@Co₃O₄ core-shell nanorods: in situ catalyst reconstruction toward high efficiency oxygen evolution reaction, *Adv. Energy Mater.* 11 (2021) 2101324.

[46] Y. Chen, K. Yue, J.-W. Zhao, Z. Cai, X. Wang, Y. Yan, Effective modulating of the Mo dissolution and polymerization in Ni₄Mo/NiMoO₄ heterostructure via metal-metal oxide-support interaction for boosting H₂ production, *Chem. Eng. J.* 466 (2023), 143097.

[47] Z.H. Dong, F. Lin, Y.H. Yao, L.F. Jiao, Crystalline Ni(OH)₂/amorphous NiMoO_x mixed-catalyst with Pt-like performance for hydrogen production, *Adv. Energy Mater.* 9 (2019) 1902703.

[48] C.F. Yang, K. Shen, R. Zhao, H. Xiang, J. Wu, W.D. Zhong, Q. Zhang, X.K. Li, N. J. Yang, Balance effect: a universal strategy for transition metal carbides to enhance hydrogen evolution, *Adv. Funct. Mater.* 32 (2022) 2108167.

[49] L. Zhang, Y. Zhu, Z. Nie, Z. Li, Y. Ye, L. Li, J. Hong, Z. Bi, Y. Zhou, G. Hu, Co/MoC nanoparticles embedded in carbon nanoboxes as robust trifunctional electrocatalysts for a Zn-air battery and water electrocatalysis, *ACS Nano* 15 (2021) 13399–13414.

[50] V. Vedharathinam, G.G. Botte, Direct evidence of the mechanism for the electro-oxidation of urea on Ni(OH)₂ catalyst in alkaline medium, *Electro Acta* 108 (2013) 660–665.

[51] J.Y. Zhao, Y. Zhang, H.R. Guo, J.K. Ren, H.T. Zhang, Y.H. Wu, R. Song, Defect-rich $\text{Ni(OH)}_2/\text{NiO}$ regulated by WO_3 as core-shell nanoarrays achieving energy-saving water-to-hydrogen conversion via urea electrolysis, *Chem. Eng. J.* 433 (2022) 134497.

[52] S.K. Geng, Y. Zheng, S.Q. Li, H. Su, X. Zhao, J. Hu, H.B. Shu, M. Jaroniec, P. Chen, Q.H. Liu, S.Z. Qiao, Nickel ferrocyanide as a high- performance urea oxidation electrocatalyst, *Nat. Energy* 6 (2021) 904–912.

[53] R.J. Lin, L.Q. Kang, T.Q. Zhao, J.R. Feng, V. Celorrio, G.H. Zhang, G. Cibin, A. Kucernak, D.J.L. Brett, F. Cora, I.P. Parkin, G.J. He, Identification and manipulation of dynamic active site deficiency-induced competing reactions in electrocatalytic oxidation processes, *Energy Environ. Sci.* 15 (2022) 2386–2396.

[54] Y.J. Wu, J. Yang, T.X. Tu, W.Q. Li, P.F. Zhang, Y. Zhou, J.F. Li, J.T. Li, S.G. Sun, Evolution of cationic vacancy defects: a motif for surface restructuration of OER precatalyst, *Angew. Chem. Int. Ed.* 60 (2021) 26829–26836.